

# Optoelectronic retinal prosthesis: system design and performance

J D Loudin<sup>1</sup>, D M Simanovskii<sup>1</sup>, K Vijayraghavan<sup>1,2</sup>, C K Sramek<sup>1,2</sup>,  
A F Butterwick<sup>1,2</sup>, P Huie<sup>1,2</sup>, G Y McLean<sup>3</sup> and D V Palanker<sup>1,2</sup>

<sup>1</sup> Hansen Experimental Physics Laboratory, Stanford University, 445 Via Palou, Stanford, CA 94305, USA

<sup>2</sup> Department of Ophthalmology, Stanford University School of Medicine, 300 Pasteur Drive, Stanford, CA 94305, USA

<sup>3</sup> Optobionics, Corp. 2462 Embarcadero Way, Palo Alto, CA 94303, USA

Received 31 October 2006

Accepted for publication 29 January 2007

Published 26 February 2007

Online at [stacks.iop.org/JNE/4/S72](http://stacks.iop.org/JNE/4/S72)

## Abstract

The design of high-resolution retinal prostheses presents many unique engineering and biological challenges. Ever smaller electrodes must inject enough charge to stimulate nerve cells, within electrochemically safe voltage limits. Stimulation sites should be placed within an electrode diameter from the target cells to prevent ‘blurring’ and minimize current. Signals must be delivered wirelessly from an external source to a large number of electrodes, and visual information should, ideally, maintain its natural link to eye movements. Finally, a good system must have a wide range of stimulation currents, external control of image processing and the option of either anodic-first or cathodic-first pulses. This paper discusses these challenges and presents solutions to them for a system based on a photodiode array implant. Video frames are processed and imaged onto the retinal implant by a head-mounted near-to-eye projection system operating at near-infrared wavelengths. Photodiodes convert light into pulsed electric current, with charge injection maximized by applying a common biphasic bias waveform. The resulting prosthesis will provide stimulation with a frame rate of up to 50 Hz in a central 10° visual field, with a full 30° field accessible via eye movements. Pixel sizes are scalable from 100 to 25  $\mu\text{m}$ , corresponding to 640–10 000 pixels on an implant 3 mm in diameter.

(Some figures in this article are in colour only in the electronic version)

## 1. Introduction

Many cases of intractable vision loss arise from selective photoreceptor degeneration. Retinitis pigmentosa (RP), for example, causes the loss of up to 95% of the photoreceptor layer, but spares up to 80% of the inner nuclear layer and ~30% of the ganglion cell layer [1, 2]. Similarly, patients with age-related macular degeneration (AMD) can lose up to 70% of photoreceptors with no loss of other retinal cell types. Approximately 1 in 4000 newborns inherits the genotype for RP, while AMD, which arises from multiple causes including natural ageing and environmental stresses, is diagnosed in 700 000 new Americans annually. While progression of AMD can be slowed (but not arrested), no treatment currently exists for RP. Electrical stimulation may be a potential treatment in cases of selective photoreceptor loss to artificially deliver

visual information to the surviving retina, thereby bypassing the damaged neural tissue. Initial experiments have produced simple visual percepts such as spots and patterns by electrically stimulating the degenerated retina with just a few electrodes [3–5].

A large percentage of patients with age-related macular degeneration preserve visual acuity in the range of 20/400 and retain good peripheral vision. Implantation of an electronic prosthesis would be justified for such patients only if it provided substantial improvement in visual acuity. In contrast, patients with advanced retinitis pigmentosa would benefit little unless there was enough enlargement of the central visual field to allow reasonable ambulation. Normal visual acuity (20/20) corresponds to angular separation of lines by 1 min of arc [6] or spatial separation on the retina of about 10  $\mu\text{m}$ . To consistently resolve two lines separated by 10  $\mu\text{m}$  requires

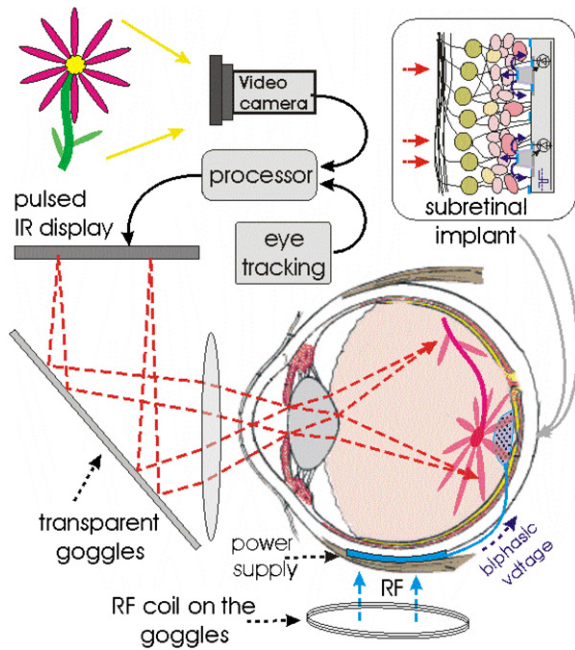


**Figure 1.** A simplified layout of the general system design including the goggles-mounted video camera, image processor and NIR display. Internally, an extraocular power supply is connected to the subretinal implant. The inset shows a magnified view of a small area of the retinal implant.

$5\ \mu\text{m}$  pixels (Nyquist sampling). Thus, visual acuity at the level of 20/400 corresponds geometrically to a pixel size of about  $100\ \mu\text{m}$ , while acuity of 20/100 (sufficient for reading with some visual aids) requires pixels smaller than  $25\ \mu\text{m}$ . It has been previously estimated that about 600 pixels is a minimum for resolving images in the central field [7] and for useful reading performance [8]. For functional restoration of sight, the array should ideally cover a field of view of at least  $10^\circ$  (which corresponds to a 3 mm diameter spot on the retina) and support a visual acuity of 20/100 (which corresponds to  $1600\ \text{pixels mm}^{-2}$ ) in the central  $2\text{--}3^\circ$  of stimulating area.

Recently, we reported a design of a high-resolution optoelectronic retinal prosthetic system [9]. In this paper, we provide a more detailed description of its components and performance characteristics.

### 1.1. System design

In our system design (figure 1), a video camera transmits  $640 \times 480$  pixel images at 25–50 Hz to a pocket PC. The computer processes the data and displays the resulting video on an LCD matrix mounted on goggles worn by the patient. The LCD screen is illuminated with pulsed near-infrared (NIR, 800–900 nm) light, projecting each video image through the eye optics onto the retina. The NIR light is then received by a photodiode array on a  $\sim 3\ \text{mm}$  implanted chip. Each photodiode converts the NIR signal into an electric current, which is injected to the retina from an electrode placed in its center. Charge injection is maximized by biasing the photodiodes using a common pulsed biphasic power supply. Since the projected NIR image is superimposed onto

a normal image of the scene observed through the transparent goggles, electrical stimulation introduces visual information into the retinal tissue above the implant, while any remaining peripheral vision responds normally to visible light. Such overlay is possible because NIR light does not activate normal photoreceptors and the implant's response to natural visible light in the eye is negligible compared to the bright and pulsed infrared image. Advantages of this system over other current approaches to visual prosthesis include the following:

- Optical projection of the images into the eye preserves the natural link between eye movements and visual information. Since the video goggles can project images onto a retinal area much larger than the chip itself, the patient can observe a larger field of view with natural eye movements rather than by scanning it with his head-mounted camera.
- Each photodiode acts as a separate data channel, allowing parallel optical transmission of information during stimulation. In contrast, single channel systems must transmit data serially, necessitating complex data decoding and memory circuitry in the implant, as well as a multiplicity of wires connecting this circuitry to the electrode array [4, 10–12].
- Adjustment of the stimulation parameters (intensity, duration and repetition rate) and the image processing algorithm can be performed for each patient without any changes in the retinal chip itself, as opposed to systems where signal processing is built into the implant [13].
- The system can be used for both epiretinal and subretinal stimulation.

A possible disadvantage of this system is that the presence of photodiodes in series with the electrodes prevents application of some types of stimulation waveforms, such as symmetric biphasic current pulses (equal current pulses of opposite polarity).

### 1.2. Stimulation threshold and proximity requirements

The threshold charge required to electrically elicit an action potential in retinal ganglion cells depends on electrode size and distance from the target cells [14, 15]. Thresholds for human perception of retinal stimulation with large epiretinal electrodes—discs of  $520\ \mu\text{m}$  in diameter—have been determined to be in the range 50–500 nC for biphasic current pulses with 1 ms per phase [5]. With electrodes of  $6\text{--}25\ \mu\text{m}$  in size placed on the epiretinal surface of the rabbit retina, the threshold for eliciting an action potential in the ganglion cells was found to be in the range of 0.05–0.3 nC [14, 16]. With  $125\ \mu\text{m}$  diameter electrodes it varied from 0.3 to 3 nC for different types of cellular responses [15]. With 0.5 ms pulses, the threshold current varied from 0.4 to  $4\ \mu\text{A}$  [15]. In subretinal stimulation using  $10\ \mu\text{m}$  electrodes and 0.5 ms pulses, the stimulation threshold was in the range of 0.4–0.7 nC, which corresponds to a threshold current of 0.8– $1.4\ \mu\text{A}$  [17].

Our first generation implant has  $100\ \mu\text{m}$  square photodiode pixels, each with a  $40\ \mu\text{m}$  diameter circular

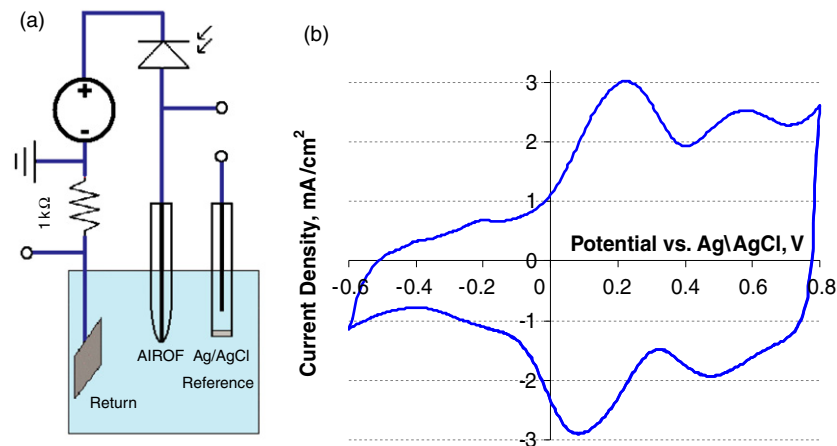


**Figure 2.** (a) Schematic of the experimental setup for measuring single pixel optoelectronic characteristics. The left terminal is used for monitoring current and the right terminals for monitoring electrode potential. (b) Cyclic voltammogram of a 75  $\mu\text{m}$  AIROF disc electrode.

electrode in its center. Based on the stimulation thresholds cited above we plan to provide 0.5 ms stimulation pulses with currents up to 20  $\mu\text{A}$  per pixel, which is five times lower than the retinal damage threshold for electrodes smaller than 100  $\mu\text{m}$  in diameter [18]. This stimulation current corresponds to 10 nC injected per pulse and a maximum electrode charge density of 0.8  $\text{mC cm}^{-2}$ . Since this charge density exceeds the safe limit for platinum electrodes (0.4  $\text{mC cm}^{-2}$  [19, 20]), we use activated iridium oxide film (AIROF) electrodes, which have a safe charge-injection limit of 1–9  $\text{mC cm}^{-2}$  [21].

Distribution of current on the surface of the metal electrode in electrolyte depends on charge-injection levels. Initially, electric current is enhanced at the edges of the disc due to enhancement of electric field at the edges of equipotential disc. However, as the electrochemical capacitance in these areas becomes fully charged (assuming that no irreversible Faradaic reactions are involved), the local current density decreases, allowing charge injection in the other parts of the electrode to ‘catch up’. Eventually, the entire electrode area is fully charged at a constant charge density. In this case, the time-average distribution of current (total charge density divided by pulse duration) is uniform across the surface of electrode. The electric field produced by a disc electrode with constant current density at its surface is nearly flat and distance independent in the near field, and spherical in the far field. The transition between the two regimes occurs at distances comparable to electrode size. In the far-field range, the electric field decreases quadratically with distance from the plane of electrode. Given that electrode–cell separation is typically 20–40  $\mu\text{m}$  for flat epiretinal and subretinal implants, our 40  $\mu\text{m}$  electrodes could effectively stimulate ganglion cells with a flat epiretinal array or inner nuclear layer cells with a flat subretinal array. The use of smaller electrodes at the same distance from the target cells would necessitate higher electrode current density to provide a similar current in the far field. Since electrochemically safe current density is limited, better proximity to target cells is essential for high-resolution stimulation. New techniques we have developed to achieve cellular-scale proximity are discussed later.

## 2. Methods and results

### 2.1. Optoelectronic characterization of different modes of operation

#### 2.1.1. Preparation and activation of IrOx (AIROF) electrodes.

The electrochemical storage capacitance of iridium electrodes can be significantly increased by electrochemical activation [21, 22]. Since electrochemical properties of such electrodes depend on their preparation, we briefly describe the activation procedure.

Iridium disc electrodes with a diameter of 75  $\mu\text{m}$  were fabricated by cutting and polishing 75  $\mu\text{m}$  iridium wire embedded in glass. The electrodes were activated by repetitive potential cycling in phosphate-buffered saline solution with a pH of 7.4. A total of 226 cycles were applied, with respect to a Ag/AgCl reference, dwelling for 10 s at each extreme (–0.6 V and +0.8 V). Later several triangle-wave cycles were included to assess the final performance and storage capacitance of the AIROF by cyclic voltammetry, as shown in figure 2(b). The electrodes were activated up to a charge storage capacity of 25  $\text{mC cm}^{-2}$ . These electrodes were subsequently connected to the photodiode and placed in Gibco’s DPBS (100  $\text{mg l}^{-1}$  anhydrous  $\text{CaCl}_2$ , 100  $\text{mg l}^{-1}$   $\text{MgCl}_2 \cdot 6\text{H}_2\text{O}$ , 200  $\text{mg l}^{-1}$  KCl, 200  $\text{mg l}^{-1}$   $\text{KH}_2\text{PO}_4$ , 8000  $\text{mg l}^{-1}$  NaCl, 2160  $\text{mg l}^{-1}$   $\text{Na}_2\text{HPO}_4 \cdot 7\text{H}_2\text{O}$ ) for further experiments.

#### 2.1.2. Characterization of photodiodes: photovoltaic or photoconductive modes, continuous or pulsed illumination.

The ‘heart’ of our system is an array of photodiodes with microelectrodes that convert light into pulsed electric current in the extracellular space, which also can be thought of as the electrolyte. We have characterized several possible aspects of the operation of our system using a photodiode connected to a microelectrode in a physiological medium.

Photodiodes illuminated by light can generate electric current, and we refer to this mode of operation as passive or photovoltaic. When an external bias voltage is applied, photodiodes conduct current well in one polarization and act as a variable, light intensity-controlled current limiter in the other. In the absence of light, only a minor ‘dark’ current

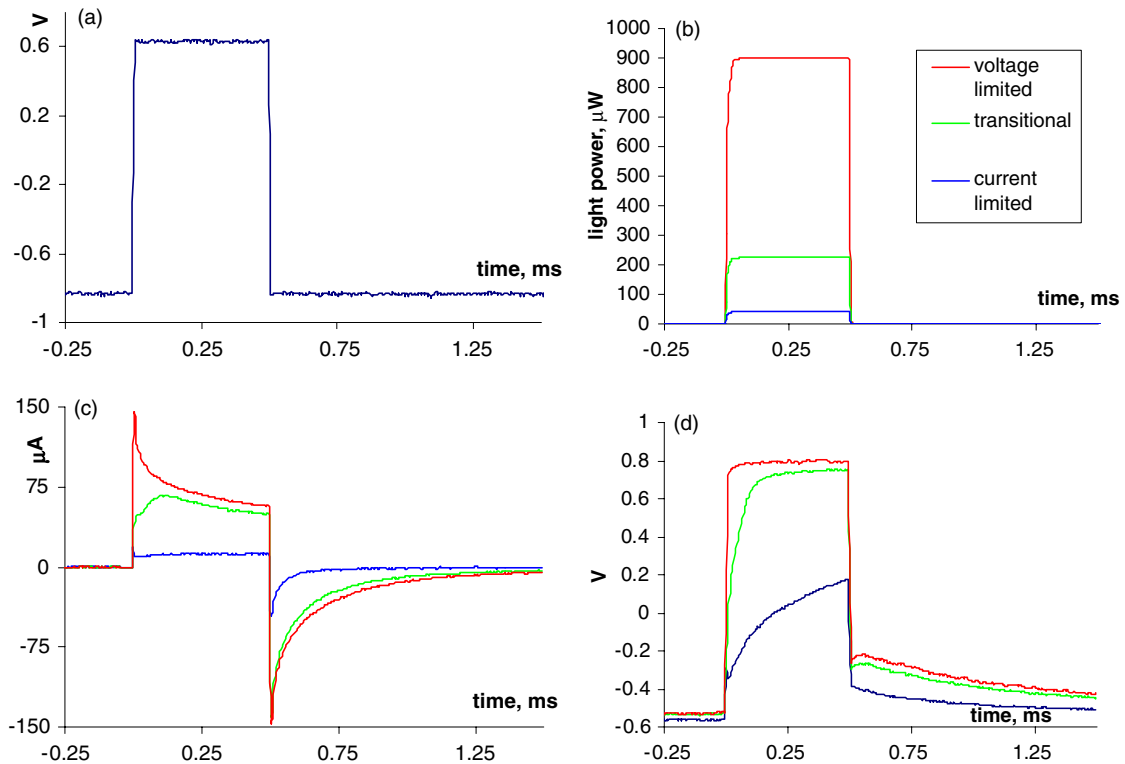


**Figure 3.** Stimulation waveforms for a  $75\ \mu\text{m}$  AIROF disc electrode actively driven in the pulsed illumination mode. Shown are (a) the bias voltage, (b) incident light power, (c) current and (d) electrode potential with respect to Ag/AgCl. Two regimes are visible: current limited and voltage limited, with a transitional waveform in between. The  $\sim 0.2\ \text{V}$  shift between the driving and electrode voltages is due to the superposition of three factors: the photovoltage, the diode voltage drop and the  $\sim 0.25\ \text{V}$  equilibrium voltage of the return electrode.

can flow under reversed bias. However, under illumination, photons absorbed in the semiconductor create free carriers (electrons and holes) that can conduct electric current across the photodiode. The amount of free carriers and thus maximal electric current is proportional to light intensity. We will refer to this mode as active or photoconductive.

There are two options for illumination in the photoconductive mode: continuous and pulsed. In the continuous illumination mode, a reversed bias is applied to photodiodes most of the time, so their conductivity and associated charging of the electrode electrochemical capacitance is controlled by local light intensity. During the short (0.5 ms) voltage pulse of conducting polarity, the photodiodes inject the accumulated charge into the electrolyte. In the pulsed mode, the reversed (non-conducting) bias is applied during the short (stimulating) pulse of light, and thus the injected current is controlled by the light intensity during this pulse. Between the short pulses, the power supply applies a conducting bias, so that electrodes are charged to the bias level without illumination.

Under both schemes it is advantageous to bias the electrodes to one end of the ‘water window’ ( $-0.6\ \text{V}$  or  $+0.8\ \text{V}$  with respect to Ag/AgCl [23]) to maximize charge injection. Since there are ohmic losses across the electrolyte, voltages outside the water window would be necessary to fully charge the electrodes to their safe limits. Indeed, some designs call for up to  $\pm 7\ \text{V}$  [24]. While these designs do fully charge the electrodes, they have an inherent risk of accidentally applying voltages outside the water window. This is because access

resistances can change over time [25] as cells reorganize, and ohmic voltage drops can also depend strongly on the location within the array of the stimulating electrode (see section 2.2). The variance in resistive drops makes it likely that the voltage drop across the electrode exceeds safe levels at some point during long-term operation. We therefore adopt a more conservative strategy of limiting the electrode potentials to within the water window to avoid the possibility of electrolysis, and because it has been shown that potentials outside the safe region lead to pH change and rapid deterioration of AIROF electrodes [26, 27]. However, while safer, this strategy cannot fully charge the electrodes by ignoring ohmic losses.

Figure 2(a) illustrates the configuration of our model circuit, a single pixel in the array, which we used to evaluate optoelectronic performance of our system. A passive (photovoltaic) system was simulated by connecting the electrodes through a photodiode to a large return electrode. An active system was simulated by placing a voltage generator between the return and the photodiode providing 0.5 ms pulses of bias voltage at 50 Hz. In all cases, illumination was provided by a laser diode emitting red light at 650 nm wavelength. A 650 nm beam was used instead of an NIR laser for ease of alignment. Performance at any NIR wavelength can then be estimated from the diode spectral response curve. In a small subset of experiments we compared 650 nm to two near-IR wavelengths, as described later.

In the pulsed illumination mode, we observed two distinct regimes of light-to-current conversion: the current-limited and voltage-limited, as shown in figure 3 and described below.

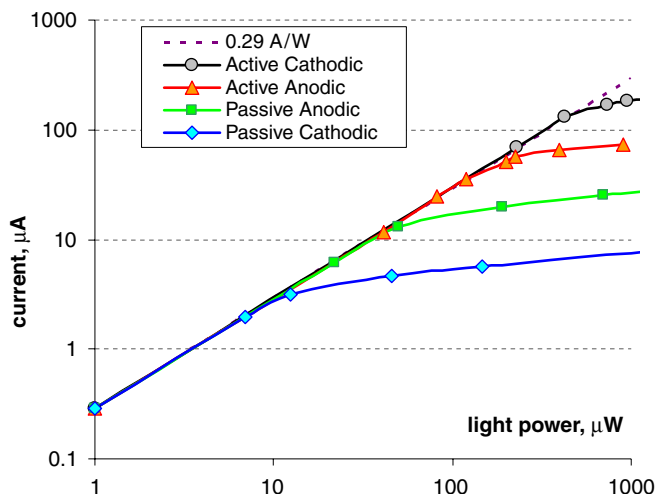


**Figure 4.** Stimulation current as a function of peak light intensity for a single,  $75\ \mu\text{m}$  AIROF pixel driven in the pulsed illumination mode. The dashed line depicts the  $0.29\ \text{A W}^{-1}$  photodiode conversion efficiency.

Figure 3 presents the results for anodic bias pulses. In the current-limited regime, the current is proportional to light intensity, thus constant light intensity is converted into a constant current during the reverse bias phase (blue lines in figure 3). The electrode potential increases gradually as the electrochemical capacitor charges from  $-0.6\ \text{V}$ , and when the electrode has been fully charged to the voltage limit, the current starts decreasing, as shown by green and red curves in figure 3. The voltage limit is given by the sum of the bias and the diode's photovoltage. At very high light intensities, the electrode reaches the voltage limit very quickly causing the current to decrease during most of the pulse (red lines). The 'recovery' pulse of current during the conductive biasing phase has the same shape regardless of the light intensities (negative-going pulses in figure 3(a)).

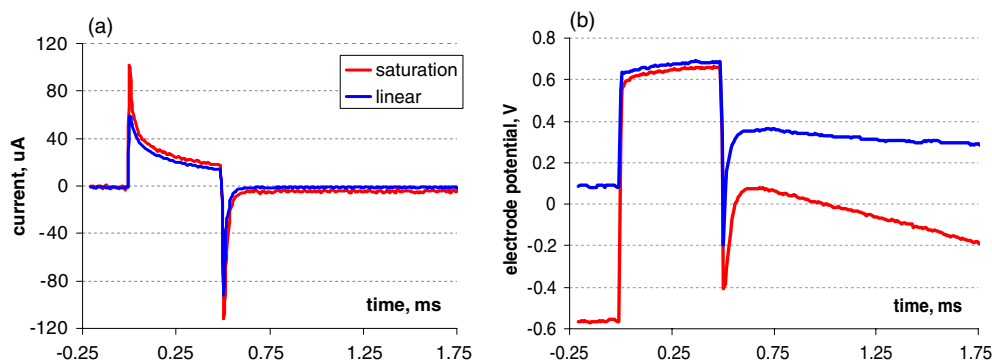
Since in our system information about stimulating current in each electrode is transmitted to each pixel as a local light intensity, linear conversion of light into current in the photodiodes is very important. Strong deviation of the light-to-current conversion from a linear relationship will make transfer

of information very difficult, if not impossible. The width of the linear range practically determines the dynamic range of stimulating currents provided by the system.

Current as a function of light power is plotted in figure 4. In the current-limited regime, the curves are all linear with a slope given by the  $0.29\ \text{A W}^{-1}$  photodiode conversion efficiency (dashed line). The voltage-limited regime corresponds to the final logarithmic behavior of the curves. This final slow rise is due to the logarithmic dependence of the photovoltage on light intensity [28]. In the logarithmic regime current depends on light intensity very weakly, thus this regime is impractical for encoding information.

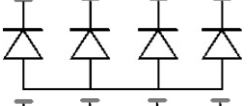
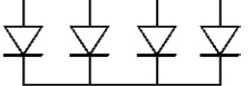
Since the photovoltage is typically about  $0.4\ \text{V}$ , the electrode in the passive system cannot be charged to the levels available in an actively biased system, and thus yields much lower charge injection. The equilibrium potential of AIROF is typically around  $0.25\ \text{V}$  with respect to  $\text{Ag}/\text{AgCl}$  [21], and it has more charge capacity above this potential than below it (see AIROF cyclic voltammogram in figure 2(b)); therefore, the passive anodic-first scheme has a higher charge-injection limit than the passive cathodic-first scheme. In the active system, the biasing phase immediately shifts the electrode potential to within a  $0.2\text{--}0.4\ \text{V}$  (a diode voltage drop) of its bias potential. It takes between 5 and 20 ms to recharge the last few hundred millivolts. For the anodic-first pulses, this slow recharge occurs between  $-0.6$  and  $-0.2\ \text{V}$  (figure 2(c)); for cathodic-first pulses it is between  $0.3$  and  $0.8\ \text{V}$ . Since there is much more charge storage capacity in the interval between  $0.3$  and  $0.8\ \text{V}$ , charge injection for the cathodic-first system is roughly three times that of the anodic-first, as shown in figure 4.

The continuous illumination mode uses the reversed bias (current-limited regime) of the diode to slowly charge the electrochemical capacitance of the electrode, and the conducting polarization to rapidly discharge it. Results for anodic-first stimulation pulses are shown in figure 5. The advantage of this technique is that it requires much less peak light power, as current is slowly delivered with continuous illumination over 20–40 ms, rather than all at once in a  $0.5\ \text{ms}$  pulse. However, average light power is about the same, since in both cases  $1\ \mu\text{J}$  of light energy is required to



**Figure 5.** Stimulation waveforms for a  $75\ \mu\text{m}$  AIROF disc electrode actively driven in the continuous illumination mode, showing (a) current and (b) electrode potential with respect to  $\text{Ag}/\text{AgCl}$ . Two regimes are visible: the linear and saturation regimes. The transition between the two is sharp; there are no transitional waveforms.

**Table 1.** Summary table of the different optoelectronic operating modes. Note that both anodal-first and cathodal-first stimulation pulses are available regardless of diode orientation. Currents are calculated for 0.5 ms pulses on 40  $\mu\text{m}$  activated iridium oxide electrodes.

Diode orientation	Illumination mode	Active bias	Stimulation pulse polarity	Maximum current
	Active pulsed	Yes	Cathodal-first	37 $\mu\text{A}$
	Passive pulsed	No	Cathodal-first	0.88 $\mu\text{A}$
	Continuous	Yes	Anodal-first	9.4 $\mu\text{A}$
	Active pulsed	Yes	Anodal-first	15 $\mu\text{A}$
	Passive pulsed	No	Anodal-first	3.4 $\mu\text{A}$
	Continuous	Yes	Cathodal-first	28 $\mu\text{A}$

deliver 0.29  $\mu\text{C}$  to the electrochemical capacitor. Current as a function of light power for the continuous illumination mode is plotted in figure 6. The slope of the linear part is about 11  $\text{A W}^{-1}$ , which corresponds to a photodiode conversion efficiency of about 0.3  $\text{A W}^{-1}$ , similar to the value measured with the voltage-biased system. The saturation regime begins at about 33  $\mu\text{A}$  for anodic-first pulses and 100  $\mu\text{A}$  for cathodic-first pulses. Unlike the voltage-biased system, there is no transitional region, but rather a sharp transition point where the photocurrent is sufficient to fully charge the electrode. Table 1 summarizes the six modes and their corresponding polarizations and maximal current injection.

It should be emphasized that though photodiode polarity is hardwired into the implant, both anodic-first and cathodic-first stimulation pulses are available. This is a consequence of the duality of the pulsed and continuous modes: pulsed illumination uses the photo-conducting (reverse) polarity for stimulation, while continuous illumination uses the conducting (forward) polarity for stimulation. Thus, no matter which direction the photodiodes are wired, one mode provides anodic-first pulses and the other provides cathodic-first pulses. The user or clinician could choose between the two modes by flipping a switch on the controller. Since it is not yet known which polarity will be most suitable for stimulation of different cells, having a system that allows both options is very convenient.

### 2.1.3. Charge-injection limits in various modes of operation.

The maximal charge injection in the linear range of the passive (photovoltaic) mode was 0.13 and 0.035  $\text{mC cm}^{-2}$  for anodic- and cathodic-first pulses, respectively. For the active pulsed illumination mode it was 0.58 and 1.5  $\text{mC cm}^{-2}$ . With continuous illumination the numbers were just slightly lower: 0.37 and 1.1  $\text{mC cm}^{-2}$ . Recalibrating these data for 0.5 ms pulses on 40  $\mu\text{m}$  electrodes gives maximal currents of 3.4 and 0.88  $\mu\text{A}$  for the photovoltaic mode, 15 and 37  $\mu\text{A}$  for the active pulsed mode, and 9.4 and 28  $\mu\text{A}$  for the continuous mode. If stimulation thresholds are sufficiently low—under 0.1  $\text{mC cm}^{-2}$  or 1 nC [15, 16, 29]—the passive system could suffice for stimulation within a limited dynamic range. For a wider dynamic range or if the retina has a higher stimulation threshold [11, 30] an active system will be required.

**2.1.4. Photodiode array measurements.** To verify light-to-current conversion efficiency of the silicon photodiode

array, we performed similar measurements at three different wavelengths: 640, 780 and 850 nm. Since microelectrodes on the array are not accessible for direct measurement of the electric potential in the medium, we only measured the current as a function of light intensity. Conversion efficiency at 640 nm was 0.30  $\text{A W}^{-1}$ —similar to our results with a single photodiode described above. At near-infrared wavelengths—780 and 850 nm—conversion efficiency was 0.35 and 0.30  $\text{A W}^{-1}$ , respectively. Thus, at 810 nm wavelength we expect to operate with a conversion efficiency between 0.3 and 0.35  $\text{A W}^{-1}$ .

### 2.2. Layout of the electrode array

The size and placement of the active and return electrodes in the array determine the spatial distribution of electric field in the tissue. Since all pixels are activated simultaneously the resulting electric field is a linear superposition of the fields produced by all the electrodes, which can cause many undesirable effects.

A simplified, analytically solvable model is useful to derive basic scaling laws. We start by considering a sphere (rather than a disc) emitting current from its whole surface at the same current density as the real implant (20  $\mu\text{A}$  per 100  $\mu\text{m}$  pixel). In this case, the total current injected from the sphere increases quadratically with its radius  $I \sim r^2$ , while the resistance between the spherical electrode and infinity decreases reciprocal to its radius  $R \sim 1/r$ . Thus, the resistive potential drop between the sphere and the return at infinity,  $U = I \cdot R$ , will increase linearly with its radius,  $U \sim r$ . Since the total number of pixels  $N \sim r^2$ , we have the scaling law  $U \sim N^{1/2}$ . Consequently, an increase in the size of the electrode array or the number of simultaneously activated pixels (assuming constant current per pixel) is accompanied by an increase in resistive voltage drop in the electrolyte. Given that our driving voltage is limited ( $-0.8$  to  $0.6$  V with respect to Ag/AgCl), these larger resistive losses decrease the potential available at the electrode/electrolyte junction and thus the attainable charge injection.

Numerically solving the three-dimensional distribution of the electric field in front of the planar electrode array is a computationally intensive task, as the required computational resources rapidly increase with the number of pixels. We used the FEMLAB 3.1 software package with the Lagrange quadratic element type, conjugate gradient linear solver, algebraic multigrid preconditioner and with the number of

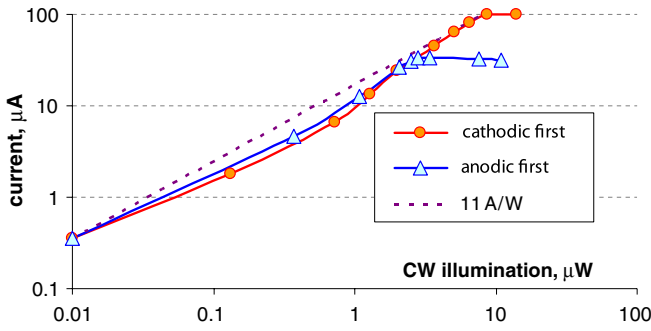


**Figure 6.** Stimulation current averaged over a 0.5 ms pulse as a function of light intensity for a 75  $\mu\text{m}$  AIROF disc electrode actively driven in the continuous illumination mode.

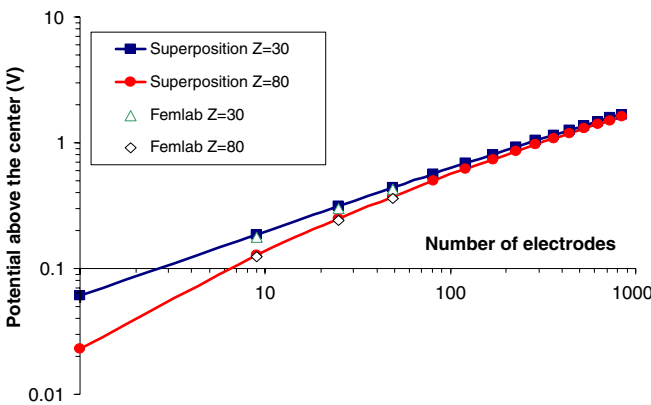


**Figure 7.** Electric potential above the center of the array as a function of number of pixels. The plots show values calculated with Femlab for arrays of 9, 25 and 49 pixels (empty symbols), and with a superposition method for arrays with up to 841 ( $29 \times 29$ ) pixels (solid lines and symbols).

nodes limited to 500 000. The largest array that could be simulated directly on the computers available to us was  $7 \times 7$ . We appealed to the principle of superposition in order to simulate larger arrays. In this approach, we first calculated the electric field due to a single electrode with constant current density on its surface which is placed in the center of a large hemispherical medium with the same resistivity as saline,  $60 \Omega \text{ cm}$  [31, 32]. To simulate the effect of multiple pixels we superimposed multiple copies of this electric field, each shifted in space by an appropriate amount. This method is applicable only when we consider electrodes with constant current densities and returns at infinity. It breaks down for surfaces maintained at constant potential because potentials are affected by the presence of other pixels. Using this simulation technique, we calculated the potential at 30 and 80  $\mu\text{m}$  above the center of planar arrays of 40  $\mu\text{m}$  circular electrodes with 100  $\mu\text{m}$  spacing and  $1.6 \text{ A cm}^{-2}$  surface current density. All potentials were calculated with respect to a ground at infinity; consequently, they are a direct measure of the resistive losses in the electrolyte. As shown in figure 7, the potentials increase with the number of pixels asymptotically approaching a  $P \sim N^{1/2}$  scaling law.

Not only do the required voltages increase with the number of pixels, they can also vary with position on the array.

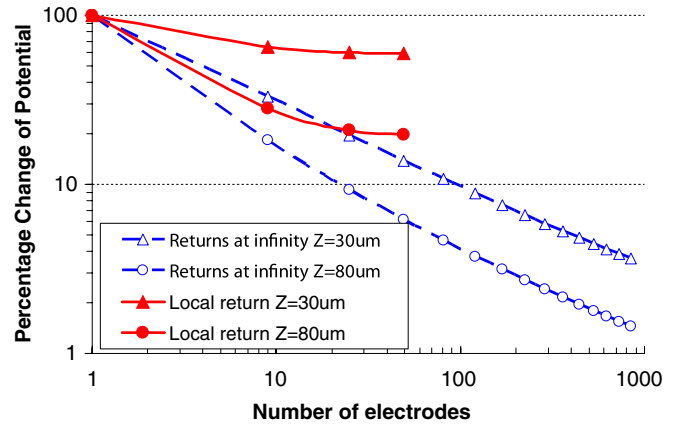


**Figure 8.** Relative change of potential (%) at 30 and 80  $\mu\text{m}$  above the central pixel when it is turned OFF, while other pixels remain ON. Values for return at infinity are calculated using the superposition method, while the values for local returns are calculated using direct Femlab modeling.

If the stimulus currents induce significant potential gradients in the medium, neighboring pixels affect one another through their combined influence on the potential. One result is that the voltage required to drive a pixel is greater if one or more of its neighbors are simultaneously driven; if all pixels are driven with the same voltage, those with more neighbors will tend to deliver less current. The effect is more pronounced for pixels in the center of an array, since they have more close neighbors. For example, with a distant return and a  $3 \times 3$  array of pixels each supplying the same current, the potential at a central pixel is 13% higher than that at the edge; in a  $29 \times 29$  array it is twice as high. Since we propose to drive all pixels with the same bias voltage, it may be important to suppress this effect by introducing local returns.

In addition to resistive effects, a system with a return at infinity experiences significant interference effects. A useful way of quantifying interference is by calculating the relative change in electric potential in front of one of the electrodes when it is turned from ON to OFF, while all other electrodes are ON. We performed such calculations for arrays which have between 1 and 841 ( $29 \times 29$ ) electrodes, all with the same constant current and with a return electrode at infinity. As shown in figure 8, the change in electric potential at 30 and 80  $\mu\text{m}$  above the central pixel rapidly decreases with the number of pixels in the array. In the  $29 \times 29$  array (a size similar to the device we intend to use), the potential changes by only 3% at 30  $\mu\text{m}$  above the implant.

Both interference and resistive effects can be greatly decreased by introducing local returns around each electrode. Figure 9(a) depicts distribution of electric potential in front of the  $7 \times 7$  array of 40  $\mu\text{m}$  disc electrodes with constant current density, interlaced by a square grid return electrode which is 10  $\mu\text{m}$  thick with a 100  $\mu\text{m}$  period. For comparison, figure 9(b) shows the electric potential in front of the same array with a return at infinity (the grid of return electrodes was treated as an insulator in this case). With local returns the electric field is very close to zero at the return grid between the pixels, so the resistive potential drop becomes independent of the number of activated neighbors.

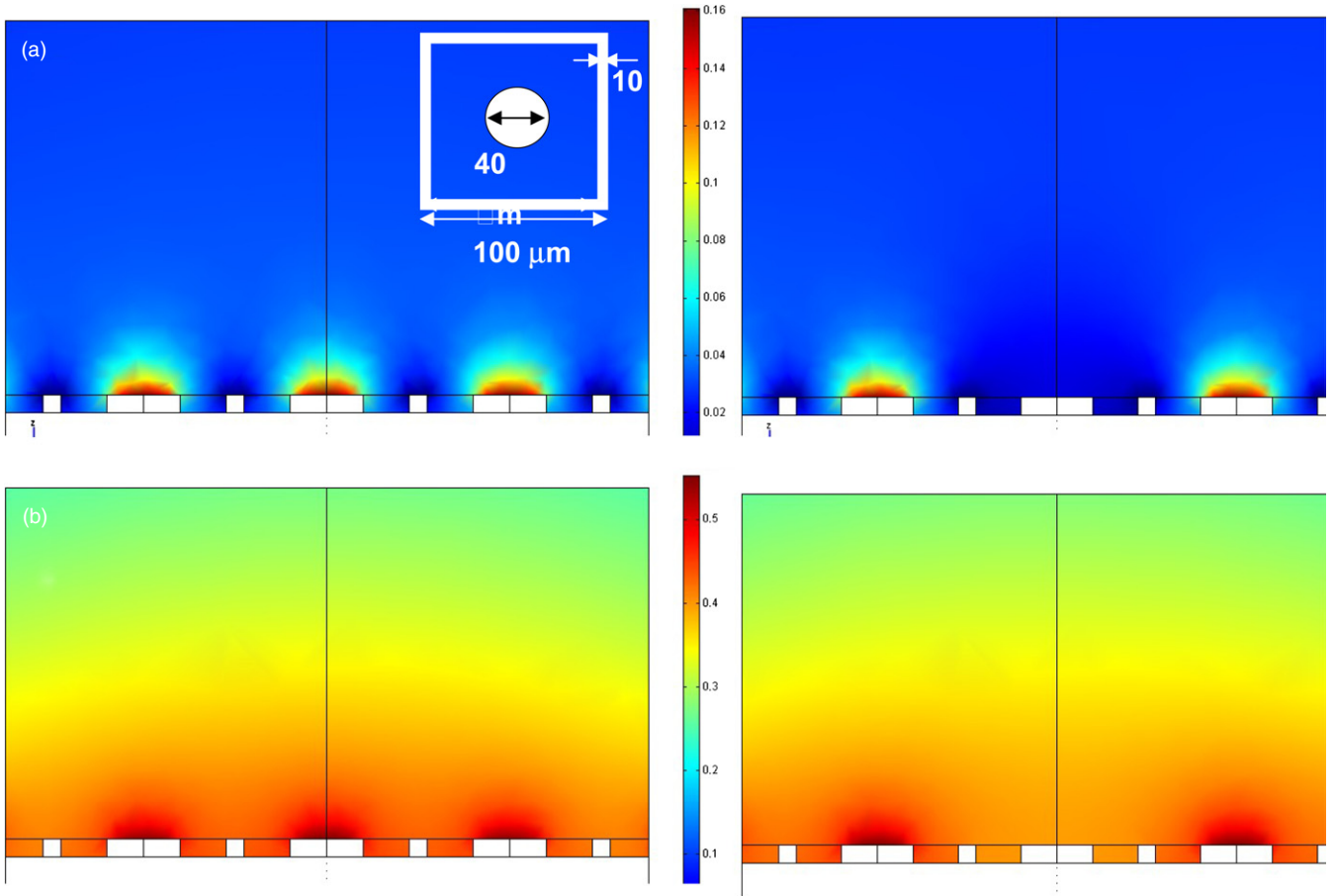


**Figure 9.** Electric potential in front of a  $7 \times 7$  array with constant current density on the  $40 \mu\text{m}$  disc electrodes: (a) corresponds to local returns and (b) corresponds to returns at infinity. Left frames show the fields when all electrodes are ON and the right frames correspond to the case when the central pixel is turned OFF. The color bar on the right of each frame shows the false color scale ranging from 0 to maximum. The inset in the upper left frame shows geometry of a single pixel.

Interference from neighboring electrodes is also decreased, as shown in figure 8. For example, at  $30 \mu\text{m}$  in front of the  $3 \times 3$  array the change of potential due to turning the central pixel OFF is 65%, and decreases to 60.4% and 59.6% when array size is increased to  $5 \times 5$  and  $7 \times 7$ , respectively. Due to the limited computational resources available we could not calculate these values for larger arrays, but it is clear that with a local return the interference effect levels off at around 60%, unlike a system with a return at infinity.

Unfortunately, the same mechanism which reduces interference also reduces the field's penetration depth into the tissue. To quantify this effect, we calculated the electric field in front of a single pixel for both a local grid return and a return at infinity. The electrode potential was assigned such that the total current injected from the electrode in both configurations was the same. As shown in figure 10, the electric field from the pixel with a local return tapers off faster. The difference becomes significant only at distances greater than the electrode size. Thus, placement of a local return grid imposes more stringent requirements on proximity between electrodes and cells. A potential solution to this problem is described later.

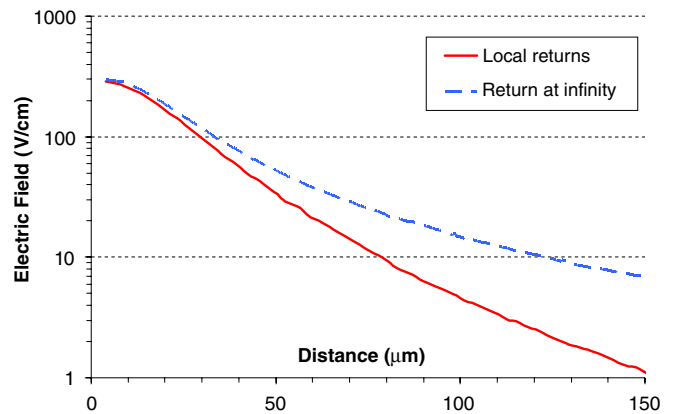


**Figure 10.** Electric field as a function of axial distance from the center of a single pixel. The dashed line corresponds to a return at infinity and the solid line to local returns. To provide similar total current, the pixel with return at infinity was held at a potential of 1 V, while that with the local return was at 0.84 V.

### 2.3. Image projection system

The projection system is designed to deliver visual information to each pixel of the retinal implant simultaneously, utilizing the



eye's natural optics. It consists of three essential parts: (a) light modulator panel which controls intensity of the light delivered to each pixel of the retinal implant; (b) illumination system, which provides uniform illumination of the light modulator within the required angular range and (c) imaging optics, which translates an image of the light modulator onto the retinal implant. The system is similar to widely available video goggles, with the exception that it delivers a thousand times (mW instead of  $\mu\text{W}$ ) more power to the eye. This difference necessitates design of a special collimating optics and use of a much brighter source of light, as described below. Like commercial goggles, they are extremely tolerant to misalignment, as the eye naturally compensates by shifting its gaze toward the visual signal.

**2.3.1. Light modulator.** As described earlier, each pixel in the retinal implant should produce 0.5 ms pulses of current with amplitudes ranging from 0.2 to 20  $\mu\text{A}$ . With a conversion efficiency of  $0.29 \text{ A W}^{-1}$ , this requires 0.5 ms light pulses with 0.7–70  $\mu\text{W}$  per pixel for the pulsed mode and continuous illumination with 0.02–2.0  $\mu\text{W}$  per pixel (at 50 Hz stimulation). A transmissive LCD or reflective LCOS panel operating in analog mode can produce video frame rate spatial light modulation with a dynamic range exceeding 100. While LCOS technology usually provides higher light throughput and better contrast, transmissive LCD panels allow a more compact system design, which is an important consideration for a system which must be worn on one's head. In our prototype system, we use a monochrome  $1024 \times 768$  pixel,  $24 \times 34$  mm LCD panel (Holoeye Photonics AG, CA), operating in analog mode with 256 levels of gray (8 bit). Depending on the polarization of the light source, the LCD display requires one or two thin film polarizers.

**2.3.2. Illumination system.** Light used in the projection system must be invisible to any remaining photoreceptors and relatively harmless to the human eye, while providing high light-to-current conversion efficiency in the implant photodiodes. Near-infrared light in the range from 800 to 900 nm satisfies all three conditions. Potential candidates for the light source in this wavelength range are light emitting diodes (LEDs) and laser diodes (LDs).

A maximum light intensity of  $P_0 = 70 \mu\text{W}$  per  $0.1 \times 0.1$  mm pixel corresponds to a retinal irradiance of  $I_0 = 7 \text{ mW mm}^{-2}$ . In the absence of optical losses, the required LCD irradiance is given by  $I = I_0 \cdot \left[\frac{f}{F}\right]^2$ , where  $f$  and  $F$  are the focal lengths of the eye and the ocular, respectively. The corresponding LCD panel surface brightness is  $B = \frac{I}{\Omega}$  where  $\Omega = \frac{\pi}{4} \cdot \left[\frac{d}{F}\right]^2$  is the acceptance angle determined by the ocular focal length  $F$  and pupil diameter  $d$ . Due to inevitable optical losses, the actual surface brightness must be significantly larger than this minimum:  $B > \frac{4I_0}{\pi} \left[\frac{f}{d}\right]^2$ . Since typically  $d \sim 3$  mm and  $f \sim 17$  mm, the minimal brightness is  $B > 0.4 \text{ W (mm}^2 \text{ Sr)}^{-1}$ . This minimum value is very close to the upper limit of the most powerful LEDs currently available. As optical losses due to absorption, reflection and geometry can exceed 90%, LEDs cannot meet the brightness

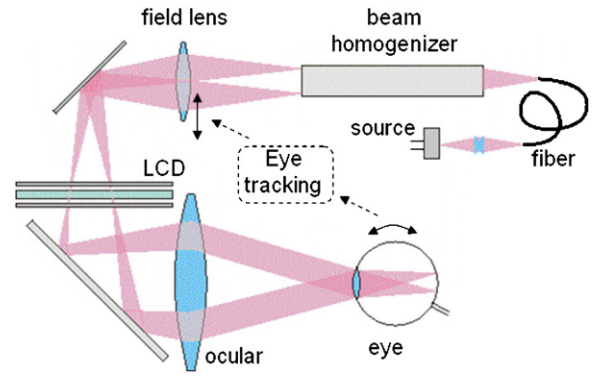


**Figure 11.** Near-to-eye projection system design. It is folded to decrease the size of the goggles. The eye tracking component is optional.

requirement. However, technological advances might make LEDs a more viable candidate for the pulsed light source in the future. LDs easily meet this brightness requirement in the near-infrared spectrum. However, the coherent nature of the light generated by a laser introduces interference patterns and speckling at the image plane.

Using a multimode LD coupled into a long stretch of a multimode fiber can greatly decrease spatial coherence of the light incident on the LCD panel. This arrangement increases the spatial frequency of the interference pattern to significantly above the pixelation frequencies of the LCD panel and retinal photodiode array. As a result, multiple speckles are averaged out on a single pixel of both the LCD matrix and photodiode array. In addition, the large pixel count of the LCD panel allows oversampling (about ten pixels of the LCD panel are imaged onto a single pixel of the implant), which further reduces interference effects. These effects decrease the pixel-to-pixel variations in light intensity on the retinal array to less than 1%, allowing full utilization of the dynamic range provided by the light modulator. Coupling multiple LD emitters into a single fiber can reduce speckling still further.

When operating at 50 Hz, the continuous illumination mode requires 2  $\mu\text{W}$  per 100  $\mu\text{m}$  pixel, which corresponds to  $0.2 \text{ mW mm}^{-2}$  retinal irradiance. This is 35 times lower than the peak irradiance required with the pulsed mode. LEDs might suffice for this mode, which would eliminate speckling and therefore simplify the design of the illumination system. However, such a system would be unable to operate in pulsed illumination mode, and therefore be much less flexible.

The projection system layout is shown in figure 11. The LD beam is shaped by a homogenizer and a field lens, which form a flat top intensity distribution and adjust the beam divergence. One possible homogenizer is a 5 cm glass bar (also known as a ‘light pipe’) with a 4 mm square cross section. An LD beam with a  $\sim 20^\circ$  divergence angle experiences several total internal reflections from the inner surfaces of the bar; the superposition of these reflected beams forms a homogenous square of light at the bar output with the same  $20^\circ$  divergence angle. The field lens images this homogenous square onto the LCD panel with  $2.5\times$  magnification, forming a  $10 \times 10 \text{ mm}^2$  illuminated area and reducing the beam

divergence to  $\sim 8^\circ$ . A second possible homogenizer is a two-layer microlens array diffuser. This homogenizer converts a collimated, inhomogeneous LD beam of arbitrary shape into a circular, homogeneous beam with a  $10^\circ$  divergence angle (RPC Photonics, NY). This beam is then projected onto the LCD screen with a field lens at 1:1 magnification. Both homogenizers provide LCD illumination with less than 10% intensity variation across the whole panel and with a specified divergence angle.

**2.3.3. Imaging system.** An ocular forms an image of the LCD panel at infinity. A  $10 \times 10 \text{ mm}^2$  area of the LCD panel seen through the  $5\times$  ocular corresponds to a  $10^\circ$  field of view, matching the angular size of the retinal implant. The distance between the ocular and the eye, or ‘eye relief’, is chosen such that the beam waist is at the eye pupil, ensuring efficient coupling of light into the eye. The 4 mm diameter of the beam waist is slightly larger than the pupil size.

The easiest way to provide a larger field of view (FOV) is by illuminating a larger area of the LCD screen. For example, illuminating a  $30 \times 30 \text{ mm}^2$  area gives a  $30^\circ$  FOV. However, this increases the light power absorbed on the retina by a factor of 9. Since the pupil translates laterally during eye rotation at a rate of about 0.18 mm/deg, a 4 mm margin between the beam size and the pupil diameter would be necessary to allow scanning of an additional  $20^\circ$  of the visual field. With a pupil size of 3 mm and beam size of 7 mm, only 18% of light will be transmitted to the retina and 82% of light will be absorbed on the iris. The associated increase in heating would bring us close to thermal safety limits (see discussion of the thermal limits in the next section). Another limiting factor is the power of the source of light—the laser diode. Losses in the optical system are quite significant: they include a factor of at least 2 on the pupil (with a beam size of 4 mm on iris), 3 on the polarizers, 2 on the LCD, 2 in the beam homogenizer and other lenses, and 2 in the fiber coupler, yielding transmission of only 2%. Delivering 40 mW maximum peak power to the retinal implant requires 2 W of peak power from the laser diode. Even though this corresponds to only 50 mW average power (again assuming 0.5 ms pulses at 50 Hz), the peak power is close to the limit for miniature laser diodes, making significant expansion of the field of view by mere increase in illuminated area and beam divergence difficult.

A better solution is to track the direction of gaze of the eye and adjust the illuminated area on the LCD screen by translating the field lens. Moving the field lens across the optical axis deflects the homogenized laser beam, thereby irradiating different parts of the LCD panel. Proper selection of the field lens focal length ensures that the deflected light beam always intersects the optical axis of the system at the point corresponding to the center of the eye. For any angular position of the eye there is a corresponding position of the field lens, ensuring constant pupil illumination. Eye tracking effectively increases the field of view to a limit (roughly  $30^\circ$  in the current design) determined only by the size of the LCD panel without using any additional light. In addition, an eye tracking system would allow the image processing software to make adjustments targeted to specific parts of the

implant to compensate for spatial variations in stimulation thresholds. Magnetic or piezo-actuators widely used for optics stabilization can perform the necessary rapid translation of the field lens.

**2.3.4. Optical safety considerations.** With maximal peak power of  $70 \mu\text{W}$  per pixel and 640 pixels in a 3 mm disc implant, the total maximal peak power on the retina is 45 mW, with  $6.3 \text{ mW mm}^{-2}$  peak irradiance. Operating with 0.5 ms pulses at 50 Hz results in a maximal average power of 1.2 mW and a maximal average irradiance of  $160 \mu\text{W mm}^{-2}$ . (In reality, the average brightness of the picture will be at least three times below the maximal level.) The peak and average retinal irradiance exceed the maximal natural levels ( $1 \mu\text{W mm}^{-2}$ ) by four and two orders of magnitude, respectively. This is one reason for operating at an invisible wavelength, where safety considerations are determined only by thermal effects. Chronic heating of a 3 mm disc by  $1^\circ\text{C}$  in water corresponds to dissipation of 7 mW of power; thus, our 1 mW will not heat it by more than  $0.2^\circ\text{C}$ , which is well within the physiological range. In fact, the temperature rise will be even smaller due to cooling by transperfusion of the choroidal blood flow [33]. According to the established safety standards [34, 35], the ED50 level for producing a minimally visible lesion in the wavelength range 810–950 nm with spot sizes exceeding 1.7 mm on the retina and exposure time exceeding 1000 s is  $5.6 \text{ W cm}^{-2}$ . Since the safety factor for maximum permissible exposure does not exceed 20 [34], the maximum permissible retinal irradiance is  $2.8 \text{ mW mm}^{-2}$ , which exceeds our required irradiance by yet *another* factor of 20. Similar thermal considerations apply to heating of the iris. With a pupil size of 3 mm and a beam diameter of 4 mm, about half of the laser power will be absorbed in the iris, causing a minute temperature rise, comparable to that on the retina. Irradiance at the cornea will not exceed  $10 \text{ mW cm}^{-2}$ , which is similar to ambient levels. Since the cornea and lens are transparent to 800–850 nm radiation no damage to these tissues is expected either.

#### 2.4. Power supply

As described above, an active bias across the photodiodes must be provided to maximize charge injection. The simplest biasing waveform is a biphasic voltage pulse: the biasing phase charges the electrode to one end of the water window, and the stimulation phase charges it to the other. This system requires both power delivery and a trigger signal, since the stimulation pulse must be synchronized with the IR light pulse. Delivering  $20 \mu\text{A}$ , 0.5 ms pulses to 640 electrodes at 50 Hz requires a 25.6 mA peak and 0.32 mA average current.

The heart of the power transmission system is a pair of inductively coupled coils. The transmitter coil is mounted beside the eye on the goggles, while the receiving coil and associated electronic circuit are implanted on the eye. We choose to operate at 1 MHz, as tissue RF absorption rapidly increases with frequency beyond a few MHz [36]. The AC current from the receiving coil is rectified using a half-wave rectifier, which collects charge into a tantalum electrolytic capacitor to provide DC to the rest of the circuit.

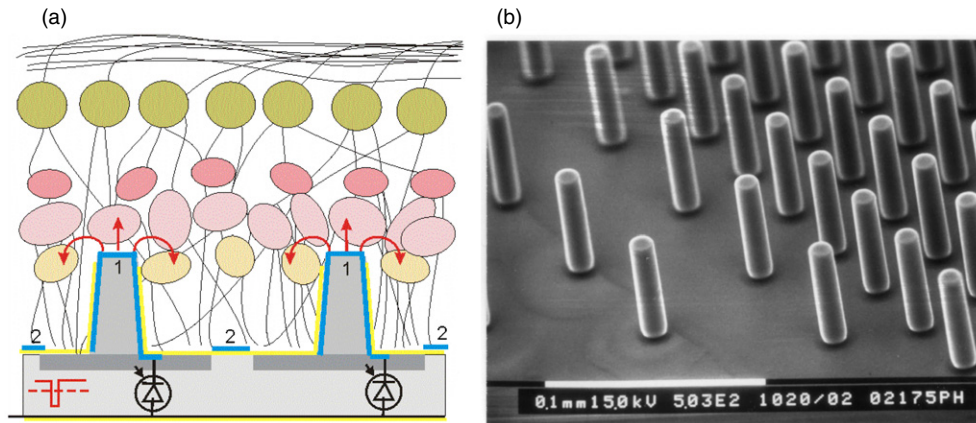


**Figure 12.** (a) A pillar array for achieving intimate electrode–cell proximity. (b) An SEM micrograph of the lithographically fabricated SU-8 pillar arrays.

As mentioned earlier, it is extremely important to keep the electrode potential between  $-0.6$  V and  $0.8$  V with respect to Ag/AgCl. Voltages even a few tens of millivolts outside of these limits lead to electrolysis, pH change and rapid electrode deterioration. To make sure the biasing voltage does not exceed the safe limits, a third, reference electrode is necessary, to keep a fixed potential with respect to the body. An additional large AIROF electrode can be utilized as a reference for controlling the bias potentials delivered to the power rails using internal shunt and series voltage regulators.

The bias switching must be synchronized with the IR light pulse within an acceptable jitter of  $\sim 10$   $\mu$ s. The signal controlling a ‘trigger bit’ is delivered over a dedicated ‘trigger’ coil operating at 500 kHz.

### 2.5. Three-dimensional implants for higher resolution

As shown in figure 10, the electric field extends into the tissue to a depth comparable to electrode size. Typical thickness of the nerve fiber layer far from the optic disc ranges from 20 to 40  $\mu$ m [37], and the ganglion cell layer from 20 to 40  $\mu$ m. An array of 40  $\mu$ m electrodes positioned right at the epiretinal surface should have sufficient proximity for electrical stimulation of ganglion cells. However, decreasing pixel size two or four times for higher resolution arrays will require proximity between electrodes and cells on the order of 20 or even 10  $\mu$ m, which is very challenging (if at all possible) in the epiretinal approach. Similarly, in degenerated retina the inner nuclear layer is typically separated from the retinal pigment epithelium by no less than 20–50  $\mu$ m of debris [38], so placing an electrode array in subretinal space will face similar proximity challenges.

This problem can be addressed by utilizing the tendency of retinal cells to migrate into porous three-dimensional subretinal implants [9, 39, 40]. Specially designed 3D implants can be used to attract cells much closer to the stimulating electrodes than they would otherwise be. For example, an array of pillars of about 10  $\mu$ m in diameter and 40–70  $\mu$ m in height with addressable electrodes at their tops and returns at the bottom would allow targeted stimulation of cells at the desired retinal depth, as diagrammatically shown

in figure 12(a). Since the pillars are vertical, and the implant is placed on the surface of the posterior pole of the eye, the pillars will face the incoming beam within a few degrees of its optical axis. Therefore they only shadow an area equal to their base, which is equal to electrode area. Thus, the shadowing with pillar electrodes will not be any different from the masking in a planar array with the same electrode size. Pillar arrays were tested using polymer implants in Royal College of Surgeons (RCS) rats. The RCS rat is a widely studied animal model of retinal degeneration in which the inability of the retinal pigment epithelium (RPE) to phagocytize shed photoreceptor outer segments leads to a progressive loss of rod and cone photoreceptors [41].

Subretinal implants were fabricated using SU-8 (MicroChem, Newton, MA), an epoxy-based photosensitive polymer, in a two-step process. First, a 45  $\mu$ m layer of SU-8 2035 is spun onto a silicon substrate and the outline of the pillar base is exposed using a contact aligner. After the base layer has been baked and unexposed regions of SU-8 have been developed away, a second layer of SU-8 2035 is deposited that defines the height of the pillar layer. Once the pillars are exposed and developed, the remaining three-dimensional pillar implants (depicted in figure 12(b)) are hard baked to complete the polymerization of the structure, remove any remaining solvents and optimize the mechanical properties of the polymer. For comparison we also manufactured flat, 45  $\mu$ m thick implants by only using the base layer of the pillar structures.

A 2–3 mm scleral incision was made 3 mm behind the limbus, on the temporal side of the eye of an anesthetized 40 days old RCS rat. A 30 gauge round tipped cannula containing sterile BSS was inserted between the retina and RPE/choriocapillaris to form a pocket by locally detaching the retina. A custom-designed implantation tool containing the implant was inserted into the pocket, at which point the implant was released and the implantation tool withdrawn. Two 11-0 nylon sutures were used to close the incision. Two and six weeks after the implantations the eyes were enucleated and quickly fixed in 2.5% glutaraldehyde, 0.9% paraformaldehyde, in 0.1 M phosphate buffer with pH 7.4, containing 3% sucrose and 1.0 mM magnesium chloride. The tissue was dehydrated

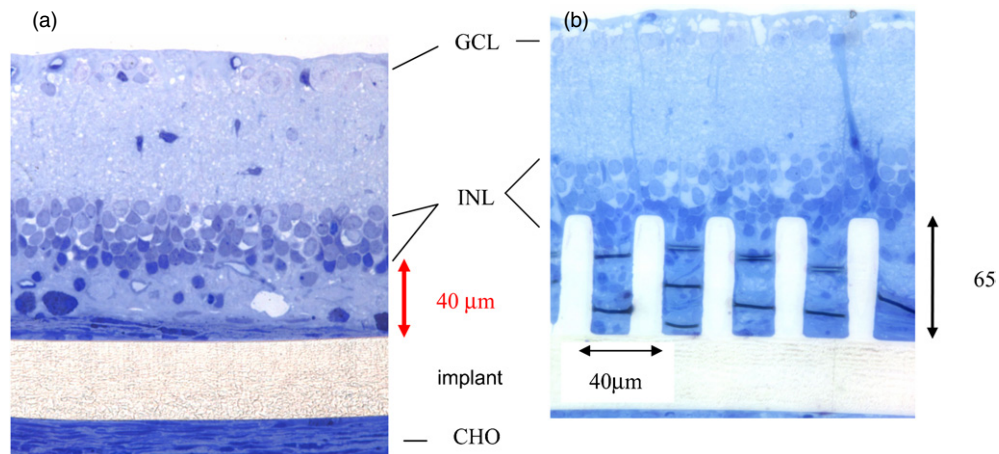


**Figure 13.** (a) Flat implant 6 weeks after implantation into P40 RCS rat. (b) Pillar array 6 weeks after subretinal implantation in a P40 RCS rat.

first in a methanol series and then with anhydrous acetone. It was infiltrated with and embedded in Eponate 12/DDSA resin (Ted Pella Inc., Redding, CA) and polymerized at 60 °C. One micron thick sections were cut on an ultramicrotome and stained with toluidine blue.

Figure 13(a) shows a histological section of an RCS rat retina with a flat, 45  $\mu\text{m}$  thick implant 6 weeks post-implantation. The photoreceptors and most of the nuclei of the outer nuclear layer have degenerated, while the ganglion cell layer (GCL), the inner plexiform layer (IPL), the inner nuclear layer (IN) with some remnant nuclei of degenerated photoreceptors still remain. The upper surface of the subretinal implant is covered with a preretinal fibrotic membrane about 10  $\mu\text{m}$  thick and a layer of hypotrophied Mueller cell processes. The inner nuclear layer is separated from the implant by approximately 40  $\mu\text{m}$ .

Figure 13(b) shows a histological section of an RCS rat retina with a pillar implant 6 weeks post-implantation. The 65  $\mu\text{m}$  pillars penetrate into the middle of the INL, while all the inner retinal layers still appear well defined. It is apparent that tissue migration around and toward the pillars during the first few days after the implantation [9, 40] provides relatively atraumatic penetration of the pillars into the INL, without significantly altering retinal architecture. In addition to providing closer proximity to the target cells, pillar structures seem to decrease the likelihood of fibrotic seal encapsulation of the electrodes. These findings should be further confirmed in the longer follow-ups and in experiments involving chronic stimulation.

Fabricating electrically active implants involves significantly more lithographic processing than their simple polymer models. In short, pillars made of a photo-definable polymer are lithographically fabricated on top of a photodiode array. The polymer pillars are then coated with a metal layer which connects them to the electrode on each photodiode. Next, an insulating layer is deposited on the sides while leaving the upper metallized surface exposed. The return electrode is a grid running between all pixels, deposited on an insulation layer on top of the photodiode array.

### 3. Conclusions

We have presented the design and specifications of an optoelectronic retinal prosthesis in which visual information is simultaneously delivered to hundreds of stimulating pixels by projecting processed video camera images onto the implant using near-infrared light. Actively biasing the photodiodes in the retinal implant increases the AIROF electrode charge injection (compared to a passive photovoltaic system) by a factor of 4 for anodic-first pulses and by a factor of 40 for cathodic-first pulses. The biphasic biasing waveform is provided by an inductively powered pulse generator placed in the subconjunctival space. Anodic-first and cathodic-first stimulation pulses are both available: one is provided by the continuous illumination mode and the other by the pulsed illumination mode. Local return electrodes surrounding each pixel decouple electric fields of neighboring electrodes thereby decreasing cross-talk and interference, but place more stringent requirements on electrode–cell proximity. Intimate proximity can be achieved using three-dimensional subretinal implants with pillar electrodes. Work is currently underway to construct a ‘first generation’ implant with 100  $\mu\text{m}$  pixels, although the same system design can be used with pixel sizes as small as 25  $\mu\text{m}$ .

### Acknowledgments

The authors would like to thank Professors Mark Blumenkranz, Michael Marmor and Ray Gariano from the Department of Ophthalmology at Stanford for useful discussions and encouragement, and Yev Freyvert for his help with implant fabrication. Funding was provided in part by the Air Force Office of Scientific Research (MFEL Program), by AMO Inc. and Optobionics Inc.

### References

- [1] Flannery J G *et al* 1989 Degenerative changes in a retina affected with autosomal dominant retinitis pigmentosa *Invest. Ophthalmol. Vis. Sci.* **30** 191–211

- [2] Stone J L *et al* 1992 Morphometric analysis of macular photoreceptors and ganglion cells in retinas with retinitis pigmentosa *Arch. Ophthalmol.* **110** 1634–9
- [3] Weiland J D and Humayun M S 2006 Intraocular retinal prosthesis. Big steps to sight restoration *IEEE Eng. Med. Biol. Mag.* **25** 60–6
- [4] Rizzo J F III *et al* 2003 Perceptual efficacy of electrical stimulation of human retina with a microelectrode array during short-term surgical trials *Invest. Ophthalmol. Vis. Sci.* **44** 5362–9
- [5] Humayun M S *et al* 2003 Visual perception in a blind subject with a chronic microelectronic retinal prosthesis *Vis. Res.* **43** 2573–81
- [6] Smith G and Atchison D A 1997 The eye *The Eye and Visual Optical Instruments* (Cambridge: Cambridge University Press) pp 291–316
- [7] Margalit E *et al* 2002 Retinal prosthesis for the blind *Surv. Ophthalmol.* **47** 335–56
- [8] Sommerhalder J *et al* 2004 Simulation of artificial vision: II. Eccentric reading of full-page text and the learning of this task *Vis. Res.* **44** 1693–706
- [9] Palanker D *et al* 2005 Design of a high resolution optoelectronic retinal prosthesis *J. Neural Eng.* **2** S105–20
- [10] Eckmiller R, Hünemann R and Becker M 1999 Exploration of a dialog-based tunable retina encoder for retina implants *Neurocomputing* **26–27** 1005–11
- [11] Mahadevappa M *et al* 2005 Perceptual thresholds and electrode impedance in three retinal prosthesis subjects *IEEE Trans. Neural Syst. Rehabil. Eng.* **13** 201–6
- [12] Hornig R *et al* 2005 A method and technical equipment for an acute human trial to evaluate retinal implant technology *J. Neural Eng.* **2** S129–34
- [13] Gekeler F and Zrenner E 2005 Status of the subretinal implant project. An overview *Ophthalmologie* **102** 941–9
- [14] Jensen R J *et al* 2003 Thresholds for activation of rabbit retinal ganglion cells with an ultrafine, extracellular microelectrode *Invest. Ophthalmol. Vis. Sci.* **44** 3533–43
- [15] Jensen R J, Ziv O R and Rizzo J F 3rd 2005 Thresholds for activation of rabbit retinal ganglion cells with relatively large, extracellular microelectrodes *Invest. Ophthalmol. Vis. Sci.* **46** 1486–96
- [16] Sekirnjak C *et al* 2006 Electrical stimulation of mammalian retinal ganglion cells with multielectrode arrays *J. Neurophysiol.* **95** 3311–27
- [17] Stett A *et al* 2000 Electrical multisite stimulation of the isolated chicken retina *Vis. Res.* **40** 1785–95
- [18] Butterwick A F *et al* Dynamic range of safe electrical stimulation of the retina *Ophthalmic Technologies vol XVI* (San Jose, CA: SPIE) **6138** 61380Q-1–8
- [19] Hesse L *et al* 2000 Implantation of retina stimulation electrodes and recording of electrical stimulation responses in the visual cortex of the cat *Graefe's Arc. Clin. Exp. Ophthalmol.* **238** 840–45
- [20] Robblee L S *et al* 1980 Electrical-stimulation with Pt electrodes: 5. The effect of protein on Pt dissolution *Biomaterials* **1** 135–9
- [21] Cogan S F *et al* 2006 Potential-biased, asymmetric waveforms for charge-injection with activated iridium oxide (AIROF) neural stimulation electrodes *IEEE Trans. Biomed. Eng.* **53** 327–32
- [22] Cogan S F *et al* 2005 *In vitro* comparison of the charge-injection limits of activated iridium oxide (AIROF) and platinum–iridium microelectrodes *IEEE Trans. Biomed. Eng.* **52** 1612–4
- [23] Troyk P R, Cogan S and DeMichele G A 2005 Compliance supply-limited driving of iridium oxide (AIROF) electrodes for maintenance in a safe operating region *10th Annual Conf. of the International FES Society Montreal*
- [24] Wang G X *et al* 2005 Design and analysis of an adaptive transcutaneous power telemetry for biomedical implants *IEEE Trans. Circuits Syst. I* **52** 2109–17
- [25] Henkin Y *et al* 2003 Changes over time in electrical stimulation levels and electrode impedance values in children using the Nucleus 24M cochlear implant *Int. J. Pediatric Otorhinolaryngol.* **67** 873–80
- [26] Brummer S B and Turner M J 1975 Electrical-stimulation of nervous-system—principle of safe charge injection with noble-metal electrodes *Bioelectrochem. Bioenerg.* **2** 13–25
- [27] Cogan S F *et al* 2004 Over-pulsing degrades activated iridium oxide films used for intracortical neural stimulation *J. Neurosci. Methods* **137** 141–50
- [28] Booth K M and Hill S L 1998 The essence of optoelectronics *Essence of Engineering* (London: Prentice-Hall)
- [29] DeMarco P J *et al* 2007 Stimulation via a subretinally placed prosthetic elicits central activity and induces a trophic effect on visual responses *Invest. Ophthalmol. Vis. Sci.* **48** 916–26
- [30] O'Hearn T M *et al* 2006 Electrical stimulation in normal and retinal degeneration (rd1) isolated mouse retina *Vis. Res.* **46** 3198–204
- [31] Geddes L A and Baker L E 1967 Specific resistance of biological material—a compendium of data for biomedical engineer and physiologist *Med. Biol. Eng.* **5** 271–93
- [32] Greenberg R J *et al* 1999 A computational model of electrical stimulation of the retinal ganglion cell *IEEE Trans. Biomed. Eng.* **46** 505–14
- [33] Schule G *et al* 2004 Noninvasive optoacoustic temperature determination at the fundus of the eye during laser irradiation *J. Biomed. Opt.* **9** 173–9
- [34] International Commission on Non-Ionizing Radiation Protection 2000 ICNIRP statement on light-emitting diodes (LEDs) and laser diodes: implications for hazard assessment *Health Phys.* **78** 744–52
- [35] Sliney D *et al* 2005 Adjustment of guidelines for exposure of the eye to optical radiation from ocular instruments: statement from a task group of the International Commission on Non-Ionizing Radiation Protection (ICNIRP) *Appl. Opt.* **44** 2162–76
- [36] Osepchuk J M 1983 *Biological Effects of Electromagnetic Radiation* (New York: IEEE) *IEEE Press Selected Reprint Series*
- [37] Frenkel S, Morgan J E and Blumenthal E Z 2005 Histological measurement of retinal nerve fibre layer thickness *Eye* **19** 491–8
- [38] Weleber R G and Gregory-Evans K 2006 Retinitis pigmentosa and allied disorders *Retina* ed J Ryan (Amsterdam: Elsevier) pp 434–36
- [39] Palanker D *et al* 2004 Attracting retinal cells to electrodes for high-resolution stimulation *SPIE, Ophthalmic Technologies vol 5314* (San Jose, CA: SPIE)
- [40] Palanker D *et al* 2004 Migration of retinal cells through a perforated membrane: implications for a high-resolution prosthesis *Invest. Ophthalmol. Vis. Sci.* **45** 3266–70
- [41] Jones B W and Marc R E 2005 Retinal remodeling during retinal degeneration *Exp. Eye Res.* **81** 123–37